ADVANCED FUNCTIONAL MATERIALS
www.afm-journal.de

The Impact of Lattice Distortions on the Magnetic Stability of Single Atoms: Dy and Ho on BaO(100)

*Boris V. Sorokin, Marina Pivetta, Valerio Bellini, Darius Merk, Sébastien Reynaud, Alessandro Barla, Harald Brune, and Stefano Rusponi**

X-ray magnetic circular dichroism, atomic multiplet simulations, and density functional theory calculations are employed to identify criteria for the optimum combination of supporting alkaline earth oxide and adsorption site maximizing the spin lifetimes of lanthanide single-atom magnets. Dy and Ho atoms adsorbed on BaO(100) thin films on Pt(100) are characterized and compared with previous results for the same two elements on MgO/Ag(100). Dy shows hysteresis in magnetic fields up to ≈3.5 T and long spin lifetime, exceeding 300 s at 2.5 K and 0.5 T. Dy displays superior magnetic stability on the bridge site than on the top-O site. Surprisingly, Ho shows paramagnetism, as opposed to its long spin lifetime on MgO. These differences originate from the local surface distortions induced by the adatoms. On MgO, minimal distortions involve only the closest O atoms, while, on BaO, they affect both the closest anions and cations. This trend reflects the decrease of the lattice energy along the series of the alkaline earth oxides, going from MgO to BaO. This study represents a step ahead in the understanding of the factors determining the spin dynamics of surface-adsorbed single-atom magnets in order to achieve their operation as qubits and memories.

1. Introduction

Lanthanide (Ln) single atoms were shown to be promising candidates for magnetic quantum technology.[1–23] Being placed on a single crystal surface or in a coordination complex, they are subject to a crystal field (CF) that lifts the degeneracy of the ground multiplet of the total angular momentum J. Careful design of the CF can result in an energy level scheme suitable for atomic-size magnetic memories[1–4,7–10,12] or quantum computation.[13,14] The spin lifetime serves as a main indicator of whether a Ln atom can be used for magnetic information storage or as a magnetic quantum bit. A CF level splitting that induces a sufficiently high magnetic anisotropy barrier can lead to long magnetization lifetimes.[21] Spin relaxation mechanisms that shortcut the anisotropy barrier are direct or assisted quantum tunneling of magnetization (QTM), which originate from level mixing induced by the finite CF symmetry. A perfectly axial CF suppresses QTM by retaining the pure character of the quantum states and therefore favors long spin relaxation times.

Among the whole Ln series, Dy and Ho exhibit the highest magnetic moments and recently have been successfully employed as single-atom[1–7,23] and single-ion magnets.[8–11] Most of these systems follow the same strategy: long relaxation times are obtained via uni-axial ligand field environments provided by one or two dominant bonds to the Ln, while the other ligands provide a marginal contribution. A family of compounds employing this strategy are the diatomic LnO complexes, which have been predicted to exhibit long relaxation times for both divalent ($4f^n$) and trivalent ($4f^{n-1}$) electronic configurations ($n = 10$ for Dy, $n = 11$ for Ho).[20–22]

So far, the closest experimental realization of an LnO unit is represented by a Ln atom adsorbed at the top-O site of MgO(100) thin films grown on Ag(100).[1–6] Indeed, for this adsorption site, the trivalent configuration of both Ho and Dy shows remarkable magnetic stability. Like MgO, other alkaline earth oxides provide a similar CF environment with the different lattice constants, ionicity, and alkaline earth metal electronegativity as potential parameters to tune the axial vs. transverse components of the CF. These properties, as reflected by the lattice energy, vary monotonically along the series of alkaline earth oxides, with BaO being of special interest since it is the furthest from MgO.[24–27]

In this article, we report on the electronic and magnetic properties of Dy and Ho single atoms adsorbed on BaO(100) thin films grown on Pt(100) single crystals and we compare

B. V. Sorokin, M. Pivetta, D. Merk, S. Reynaud, H. Brune, S. Rusponi
Institute of Physics
Ecole Polytechnique Fédérale de Lausanne (EPFL)
Station 3, Lausanne CH-1015, Switzerland
E-mail: stefano.rusponi@epfl.ch
V. Bellini
S3-Istituto di Nanoscienze-CNR
Via Campi 213/A, Modena I-41125, Italy
A. Barla
Istituto di Struttura della Materia (ISM)
Consiglio Nazionale delle Ricerche (CNR)
Trieste I-34149, Italy
The ORCID identification number(s) for the author(s) of this article can be found under https://doi.org/10.1002/adfm.202213951.

DOI: 10.1002/adfm.202213951

with previous experiments for the analogous cases on MgO/Ag(100). The samples were studied with X-ray absorption spectroscopy (XAS), XMCD, and X-ray linear dichroism (XLD). Both elements exhibit only trivalent electronic configuration. Dy adatoms show magnetic hysteresis, while Ho adatoms are paramagnetic. Combining atomic multiplet simulations and DFT calculations, we reveal that both elements adsorb with almost identical probability on top-O and on the two bridge sites of the BaO unit cell, and that all these different species contribute to the observed magnetic properties. Adatoms induce local surface distortions which are specific to both adsorption site and alkaline earth oxide. In oxides with large lattice energy, like MgO, only the closest O atoms are involved, while in an oxide with smaller lattice energy, like BaO, distortions affect both the closest anions and cations. Consequently, on BaO, adatoms on the top-O site are affected by a strong C_{4v} transverse term resulting in an inverted double-well-shaped energy scheme, while a mainly axial CF is found on MgO. Conversely, at bridge sites, local distortions turn out to be advantageous for a Kramers ion like Dy, resulting in a higher energy barrier on BaO compared to MgO, while strong level mixing is observed for the non-Kramers Ho.

2. Results and Discussion

XAS, XMCD, and XLD measurements were performed at the EPFL/PSI X-Treme beamline of the Swiss Light Source.[28] We investigated the $M_{4,5}$ edges ($3d \rightarrow 4f$ transitions) of Dy (**Figure 1**) and Ho (**Figure 2**) atoms adsorbed on BaO(100) thin films grown on Pt(100) to determine the $4f$ orbital occupation and magnetic properties of the adatoms. Our measurements were performed on five to eight monolayers (ML) thick highly crystalline BaO(100) thin films (see Experimental Section and Supporting Information); no significant differences were observed within this thickness range. The spectra were acquired at $\theta = 0°$ (normal incidence) and $\theta = 60°$ (grazing incidence) angles between the photon beam, oriented parallel to the magnetic field, and the surface normal. For simplicity of discussion, we introduce a Cartesian coordinate system with the z-axis directed along the surface normal and the y-axis perpendicular to the magnetic field (Figure 1d). From the multiplet structure of the XAS and XMCD spectra, we infer a $4f^9$ electronic configuration of Dy adatoms.[29] The XMCD spectra of Dy atoms on BaO acquired at B = 5.5 T demonstrate a slightly higher intensity at grazing than at normal incidence, hinting at easy in-plane

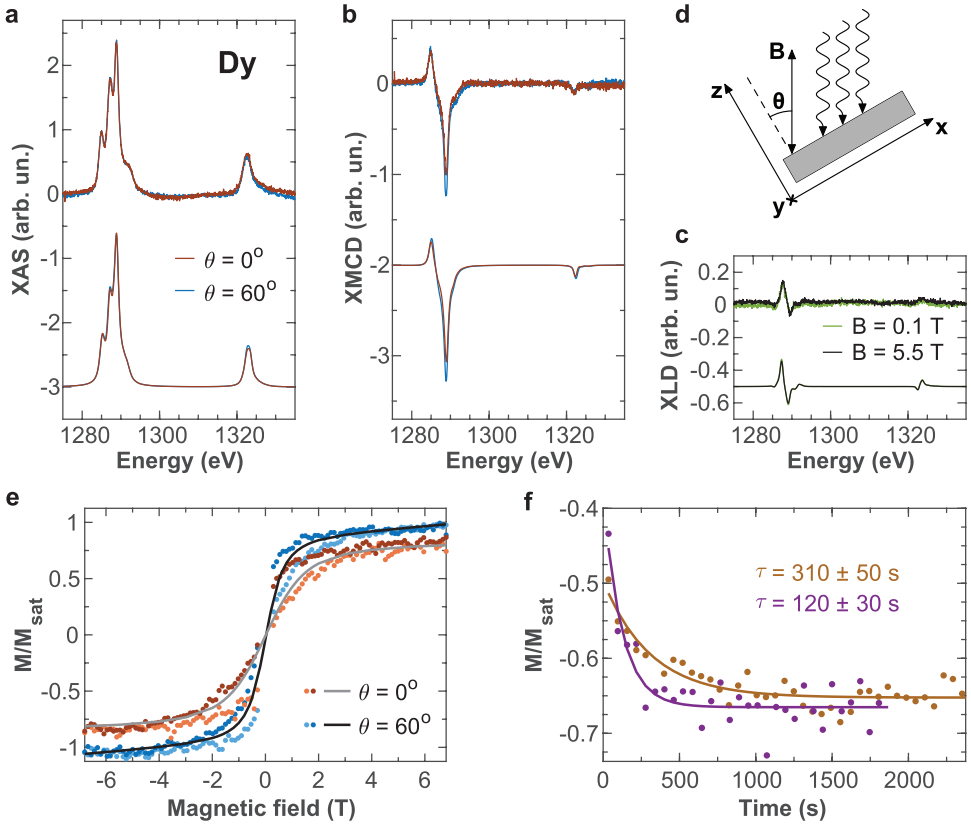

Figure 1. Experimental and simulated a) XAS, b) XMCD, and c) XLD spectra of Dy adatoms (coverage Θ_{Dy} = 0.019 ML, T_{dep} = 2.5 K) on a 5.5 ML thick BaO(100) film grown on Pt(100). XAS and XMCD spectra were measured at normal ($\theta = 0°$) and grazing ($\theta = 60°$) incidence (B = 5.5 T); XLD spectra were recorded at grazing incidence at B = 0.1 T (green lines) and B = 5.5 T (black lines). The simulated data have been vertically offset for clarity. d) Schematic representation of the experimental geometry. e) Magnetization curves measured by acquiring the XMCD signal at 1288.8 eV as a function of magnetic field ($\phi = 5.4 \times 10^{-3}$ photons nm^{-2} s^{-1}), $|\dot{B}| = 33$ mT s^{-1}). Dots denote the experimental values; the simulated equilibrium curves are shown with solid lines. f) Time evolution of the XMCD intensity at 1288.8 eV measured at grazing incidence and B = –0.5 T after saturation of the sample magnetization at B = 4 T. Dots, experimental data; lines, single exponential fits. (purple) $\phi = 9.2 \times 10^{-4}$ photons nm^{-2} s^{-1}, (ocher) $\phi = 1.4 \times 10^{-3}$ photons nm^{-2} s^{-1}). Sample temperature is T = 2.5 K for all experimental and simulated curves.

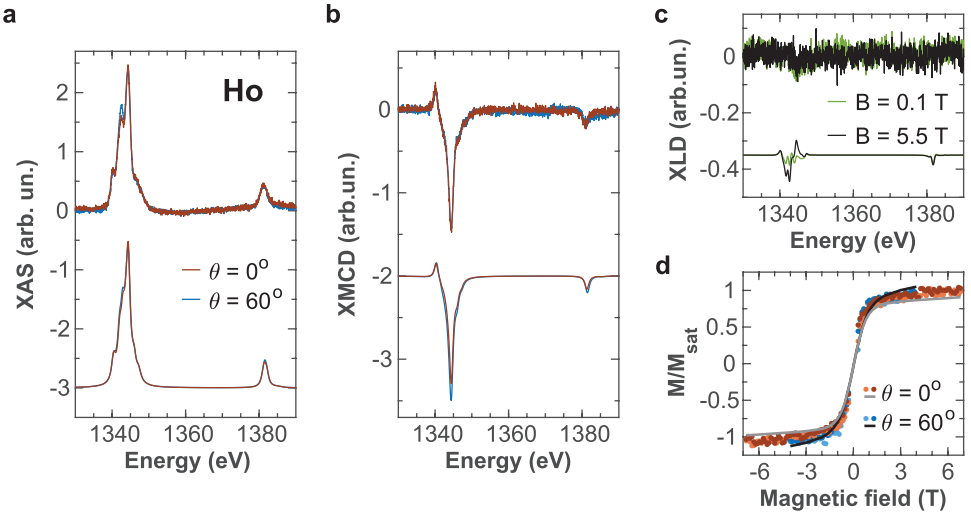

Figure 2. Experimental and simulated a) XAS, b) XMCD, and c) XLD spectra of Ho adatoms (coverage Θ_{Ho} = 0.009 ML, T_{dep} = 2.5 K) on a 5.9 ML thick BaO(100) film grown on Pt(100). XAS and XMCD spectra were measured at normal ($\theta = 0°$) and grazing ($\theta = 60°$) incidence (B = 5.5 T); XLD spectra were recorded at grazing incidence at B = 0.1 T (green lines) and B = 5.5 T (black lines). The simulated data have been vertically offset for clarity. d) Magnetization curves measured by acquiring the XMCD signal at 1344 eV as a function of magnetic field ($\phi = 4.7 \times 10^{-3}$ photons nm^{-2} s^{-1}), $|\dot{B}| = 33$ mT s^{-1}). Sample temperature is T = 2.5 K for all experimental and simulated curves.

magnetic anisotropy of the adatom ensemble. We acquired magnetization hysteresis curves by measuring the XMCD signal at the peak of the M_5 edge (1288.8 eV) while sweeping the magnetic field between ±6.8 T at the rate of 33 mT s^{-1} (Figure 1e). Both normal and grazing magnetization loops show a narrow opening, which extends up to about 3.5 T. Such hysteretic behavior is a sign of a long spin lifetime τ.[1,5,7] We followed the spin relaxation dynamics by saturating the magnetization of our sample at B = 4 T and $\theta = 60°$, then sweeping the magnetic field down to B = –0.5 T at the maximum possible rate of 33 mT s^{-1} and measuring the subsequent time evolution of the XMCD signal (Figure 1f). We find a strong photon-flux dependent relaxation time with the largest value of ≈300 s. This value is a lower bound, the intrinsic relaxation time of the system not perturbed by secondary electrons is presumably much larger.

Similarly to Dy, also Ho on BaO is found in the trivalent electronic configuration ($4f^{10}$), as can be deduced from the shape of the XAS and XMCD spectra,[29] see Figure 2a,b. The corresponding XMCD signal reveals no preferential direction for the magnetic moment of the adatom ensemble. Surprisingly, no signs of hysteresis are observed in the magnetization loops (Figure 2d).

The data show a strikingly different magnetic behavior for both Dy and Ho on BaO as compared to MgO[1,3] although the two surfaces possess several similarities. We combine DFT and multiplet calculations to identify the origin of this difference. From DFT we obtain the geometries and charge distributions of the adsorption complexes (see Supporting Information for details about DFT calculations); this information is then used to define the CF in the multiplet calculations.

The total energies, relative to the top-O site, for Dy and Ho adatoms on BaO(100) and MgO(100), as calculated from the on-site B3LYP exchange-correlation functional,[30] are reported in **Table 1**. Recent works on the magnetic properties of adatoms on thin films of MgO on Ag(100) discuss the role of the metallic support.[5,31] In particular, it was shown that Dy adatoms have a $4f^9$ configuration, due to transfer of one electron to the metallic substrate, only on MgO films thinner than 5–6 ML, while a $4f^{10}$ configuration is observed for thicker MgO films. This implies that electron tunneling to the metal support is limited to barrier thicknesses smaller than ≈1.2 nm. Our experiments focus on Ln adatoms on BaO films with thickness between 5 and 8 ML. This corresponds to barrier widths ranging from 1.4 to 2.2 nm, i.e., larger than the limit found for MgO, thus excluding charge transfer to the metal substrate. Consequently, calculations were performed using thick slabs without metallic support. The results for MgO(100) are given for comparison. The adsorption of Ln on top of the alkaline earth metal atoms, Ba and Mg, is highly unfavorable and not discussed further. While on MgO the top-O site is clearly preferred, in agreement with previous calculations,[32] on BaO the bridge site is found to be very close in energy to the top-O site, for both Dy and Ho.

The Dy 4*f* occupation reveals a tendency toward a trivalent configuration on BaO, particularly evident for the bridge site, in agreement with our experimental observations. This

Table 1. Total energies (in eV) of Dy and Ho on BaO(100) and MgO(100) (the values are relative to the top-O site of each system) for the top-O and bridge adsorption sites; occupations of the 4*f* orbital (integrated over spheres of radius of 2.4 a.u. centered on the nuclei positions) of the Ln adatoms are reported as well.

	Energy (eV)		n (e$^-$)	
System	top-O	bridge	top-O	bridge
Dy/BaO	0	0.07	9.56	8.96
Ho/BaO	0	0.03	9.93	9.93
Dy/MgO	0	0.44	9.75	9.77
Ho/MgO	0	0.65	9.93	9.92

contrasts with the divalent configuration we find on MgO, as also reported in a previous study of Dy adatoms on thick MgO films.[5] For Ho, DFT finds an occupation close to $4f^{10}$ for both substrates, in line with our observations on Ho/BaO/Pt(100) and with the experiments on Ho/MgO/Ag(100).[1] Because XMCD investigates the $M_{4,5}$ edges ($3d \rightarrow 4f$ transitions) of the Ln atoms, it provides only the occupation of the 4*f* shell, while no information is obtained on the occupation of the *spd* valence shells. DFT helps to fill this gap showing that roughly one electron moves from the 4*f* to the 5*d* shell and that the 6*s* and 6*p* shells have occupations close to the ones of free-standing atoms (see Tables S1 and S2, Supporting Information), corresponding to a trivalent configuration. Further, the Bader analysis shows that these *spd* valence electrons are mainly localized at the Ln atom, with less than one valence electron transferred to BaO for all species (see Tables S3– S6, Supporting Information).

Figure 3 shows 2D isosurfaces of the charge densities for Dy adatoms on BaO(100) and MgO(100), for top-O and bridge sites, with cross-sections at the Dy-O-Ba(Mg) and O-Dy-O planes, respectively. A striking difference is the structural deformation produced in the surface plane by Dy adsorption on BaO as compared to the minimal distortion seen on MgO, as expected based on the different lattice energies of the two oxides. On BaO, upon top-O adsorption, the O atom below Dy is pulled out of the surface and the next nearest-neighbor Ba atoms are laterally pushed away. Similarly, upon bridge adsorption, the two O nearest-neighbors are pulled out of the surface and simultaneously Dy relaxes toward the surface, thus resulting in short Dy-O distances, while the Ba next nearest-neighbors are laterally pushed away also in this case. The substrate relaxation strongly affects the local charge density distribution and consequently the CF experienced by the adatom. For top-O, we observe a high electron density along the Dy-O bond. In addition, the Ba displacement toward the O atoms sitting along the high symmetry directions produces an electron accumulation in the Ba-O bonds, with a concomitant depletion on the opposite Ba side, facing Dy. In first approximation, this charge redistribution can be seen as dipoles forming at the next nearest-neighbor Ba sites with a positive charge toward Dy. Using the same argument, the upward displacement of the O below Dy results in a dipole formation also on the Ba below Dy, in the first sub-surface plane. A similar situation is observed for the bridge site, with the Ba atoms having an excess of negative charge in the bonds formed with outer O atoms and an excess of positive charge facing Dy. In comparison, the smaller relaxation induced by Ln adsorption on MgO results in charges localized at the atom centers and only negligible interstitial charges. Calculations performed for Ho adsorbed on the two surfaces show the same behavior as observed for Dy.

We used this knowledge to perform multiplet calculations with the multiX code.[33] We considered both top-O (Ln^{top}) and bridge (Ln^{br}) adsorption sites. In the experiment, the samples have been oriented according to the sketch in **Figure 4**a with the external magnetic field in the xz plane (see Supporting Information for details on sample orientation). In order to reproduce the experimental conditions, two bridge adsorption

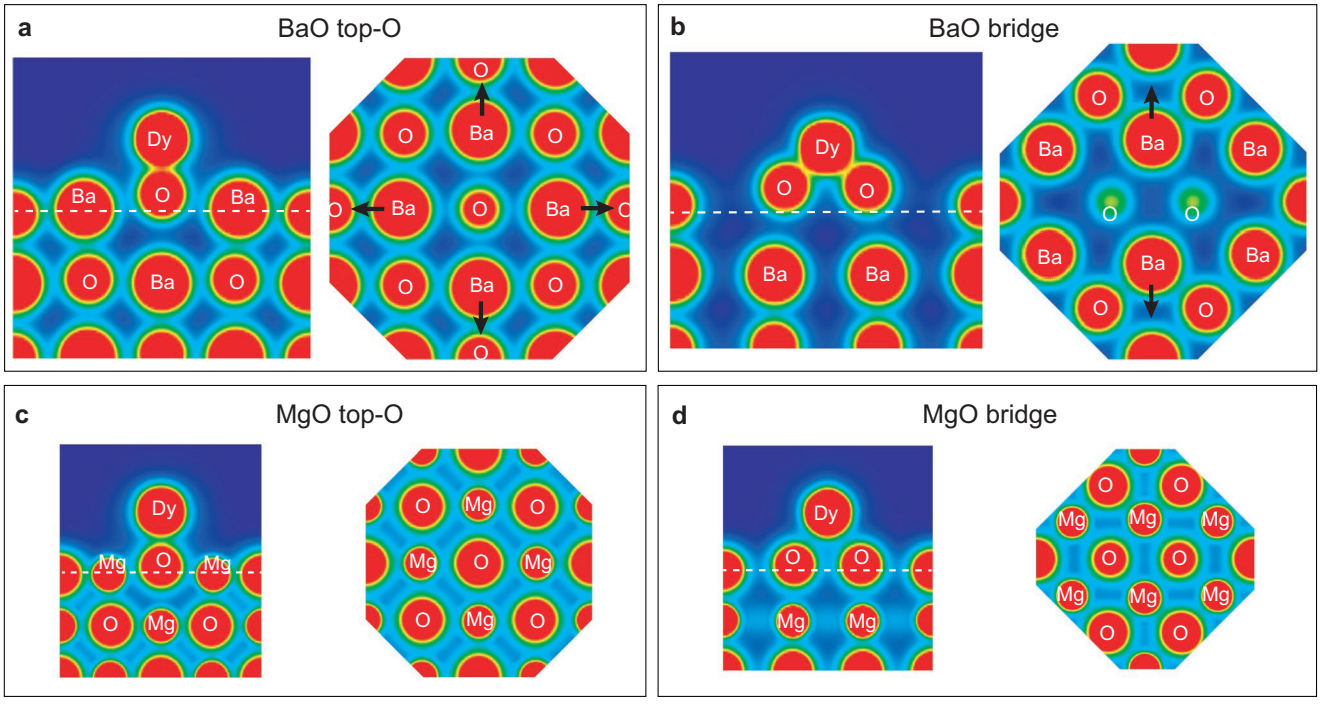

Figure 3. 2D cross sections of the charge density isosurfaces (isovalue = 0.12 $e^{-}Å^{-3}$) for Dy adatoms on top-O and bridge sites on BaO(100) (a,b) and MgO(100) (c,d). Sketch sizes are scaled according to the oxide lattice constant; sketches for bridge sites are rotated by 45° about the surface normal. Sections perpendicular and parallel to the surface plane are given on the left and right sides of each panel, respectively. Perpendicular sections correspond to the plane identified by nuclear positions of Dy, O nearest-neighbor, and Ba(Mg) next nearest-neighbor atoms. Parallel sections correspond to the plane through the nuclei of the Ba(Mg) next nearest-neighbor atoms (see white dashed line in each left panel). Black arrows highlight the Ba lateral displacement.

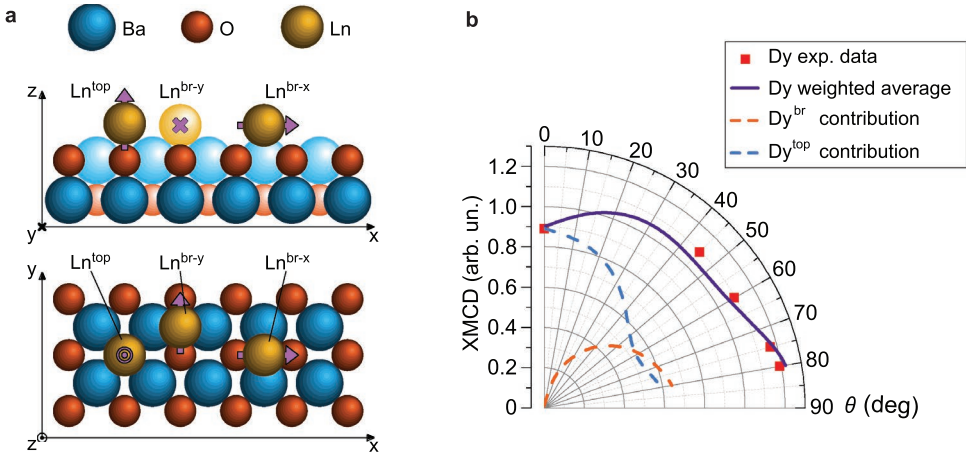

Figure 4. a) Ln adatoms at top-O, br-x, and br-y adsorption sites projected on xz and xy planes; violet arrows indicate the easy magnetization directions for the different species. Atoms depicted with lighter colors belong to the row that is shifted by half a lattice constant along the y axis. b) Experimental and calculated angular dependence of the XMCD signal at 1288.8 eV normalized to the XAS area (0.014 ML of Dy on 6.2 ML thick BaO, $B = 4$ T, $T = 2.5$ K). Red squares denote the experimental data; the purple solid curve is the calculated weighted average over all species (40% Dy^{top} + 30% $Dy^{br\text{-}x}$ + 30% $Dy^{br\text{-}y}$); blue and orange dashed curves are the calculated contributions of Dy^{top} and Dy^{br} species to the average.

sites, having different alignment with respect to the magnetic field orientation for grazing incidence measurements, were included in the multiplet calculations. The br-x adsorption site has the two nearest O atoms lying along the x axis ($Ln^{br\text{-}x}$), while the br-y one along the y axis ($Ln^{br\text{-}y}$), see Figure 4a.

MultiX uses effective point charges to compute the CF. The choice of positions and values of these charges is a recurring problem in such calculations due to the necessity of modeling the continuous spatial distribution of real charges with a few point-like ones.[34,35] Several models have been proposed in the past decades; however, a general strategy is still missing.[36–40] In the Dy/MgO case, motivated by the localized nature of the charges, the rather intuitive approach consisting in replacing the ionic charges provided by DFT by point charges of the same intensity and located at the atom centers works quite well. Only a scaling factor of 0.8 applied to the quantum level scheme is required to get good agreement with the experimental results.[3,5] On the contrary, the strong lattice relaxation and charge redistribution found by DFT entail a more elaborated approach for BaO. Therefore, we used the following procedure to construct a realistic CF: 1) the Ln-O interaction, leading to high interstitial charges, is described by an effective charge whose value (q_{eff}) and position (R_{eff}) are given by $q_{eff} = \nu_{Ln}(\varepsilon_O - \varepsilon_{Ln})/(N\varepsilon_{Ln})$ and $R_{eff} = R_O\varepsilon_O/(\varepsilon_{Ln} + \varepsilon_O)$, where ν_{Ln} is the number of electrons in the Ln valence shells, here assumed equal to the Bader charge, N the number of nearest O neighbours, R_O the Ln-O distance, and $\varepsilon_{O,\,Ln}$ the Pauling electronegativity of the corresponding element, as proposed in ref. [37]. 2) The Ln-Ba interaction is represented by an interstitial positive charge located at the ionic radius of Ba (0.149 nm) along the Ln-Ba direction, in order to mimic the dipole formation seen in DFT calculations; the value of this positive charge is used as fit parameter with the constraint that it can not exceed the Bader value. Details about atomic coordinates and Bader charges are given in the Supporting Information.

For both Ln adatoms, the top-O adsorption site results in a quantum level scheme with a reversed double well shape corresponding to a slight out-of-plane anisotropy, while the bridge site results in a O-Ln-O easy axis, see **Figures 5** and **6**. Thus, taken individually, none of the adsorption sites can reproduce the experimental data. An excellent agreement between measured and calculated spectra is found with abundances of (40 ± 4)% for top-O, and of (30 ± 2)% each for br-x and br-y, as neatly exemplified by the angular dependence of the Dy XMCD signal at 1288.8 eV shown in Figure 4b. The simulated XAS, XMCD, XLD spectra shown in Figure 1a–c, Figure 1e (Dy) and Figure 2 (Ho) agree perfectly with experiment and thus confirm our CF choice. Also the simulated thermodynamic equilibrium magnetization curves agree perfectly with the expectation from experiment if the system had no kinetic limitations caused by the finite magnetic relaxation time. The relative abundances of Ln atoms at top-O and bridge sites suggest that atoms landing on the highly unfavorable top-Ba sites diffuse with approximately the same probability to either of those sites. Indeed, from the statistics of impact sites (there are two bridge sites, one top-O and one top-Ba site per BaO surface unit cell) and in the case of equal diffusion probability from top-Ba to top-O and bridge, we infer theoretical relative abundances for these sites of 37.5% and 62.5%, respectively. These numbers agree within the error bars with the fit values and follow the trend found by DFT for the adsorption site energies (Table 1). The coexistence of Ln atoms at top-O and bridge sites is similar to the case of Ln adatoms on MgO, where adsorption on top-O and bridge sites was experimentally observed by scanning tunneling microscopy.[3,5,32] Also for Dy on the SrO termination of $SrTiO_3$ the two adsorption sites top-O and bridge coexist.[23]

The magnetic anisotropies and spin lifetimes observed for the two Ln elements can be understood with the help of the 4*f* quantum level schemes and the ground-state wavefunctions provided by the multiplet calculations for the different adsorption sites.

The quantum level schemes for Dy^{top} and $Dy^{br\text{-}x}$ projected along easy and hard axes are shown in Figure 5. The Dy^{top} and Dy^{br} ground-state wavefunctions are given in **Table 2**.

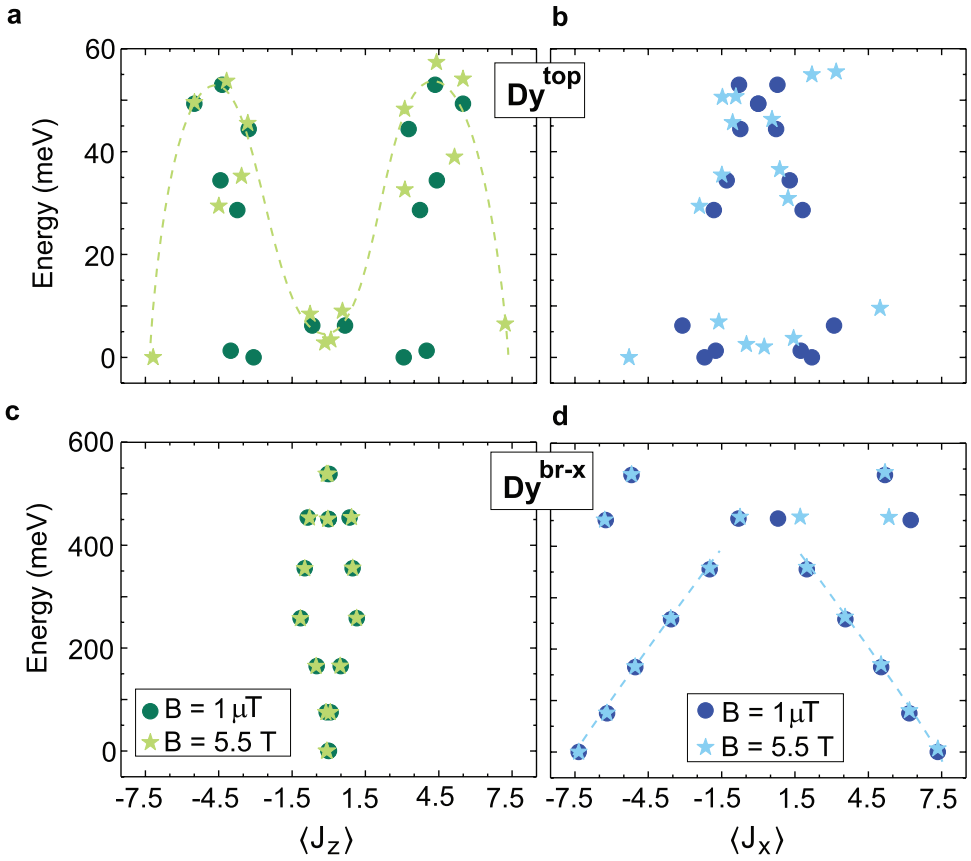

Figure 5. Quantum level scheme of the ground J multiplet for a,b) Dy^{top} and c,d) $Dy^{br\text{-}x}$ atoms on BaO in small (1 μT) and high (5.5 T) magnetic field applied along z and x axes. The dashed lines illustrate the energy barriers separating states with opposite spins.

For Dy^{top}, the C_{4v} symmetric CF mixes states whose J_z differ by multiples of 4. The mixing is particularly strong between $\left|\pm\frac{15}{2}\right\rangle$ and $\left|\mp\frac{1}{2}\right\rangle$, given their quite small energy separation of about 1 meV; this results in a ground doublet composition with an almost identical weight of these two states, providing possible shortcuts for spin reversal. Conversely, the C_{2v} symmetric bridge sites have a strong in-plane anisotropy with the maximum projection of J along the x axis (J_x) for $Dy^{br\text{-}x}$ and along the y axis (J_y) for $Dy^{br\text{-}y}$ adatoms. The ground doublet is well isolated from the first excited doublet ($\Delta E = 75$ meV); the total barrier is quite high with the states at the top of the barrier mixing with higher J multiplets, similarly to the behavior predicted for diatomic LnO complexes.[20–22] We predict the top of the barrier at more than 450 meV, a value which largely overcomes the ones reported so far, namely 180 meV for Ho/MgO[4] and 250 meV for Dy/MgO,[3] both on top-O site. As a consequence of these strong in-plane easy axes, we find only a negligible projection of the Dy^{br} spins onto the surface normal direction even in high out-of-plane magnetic fields (see the orange dashed line in Figure 4b).

The experimentally observed slight in-plane anisotropy for the atom ensemble results from the sum of the contributions of the different adsorption sites. At normal incidence the XMCD signal originates only from Dy^{top} adatoms, as the magnetic moments of both Dy^{br} species remain oriented in-plane in our experimental conditions. On the contrary, at grazing incidence the observed signal is a field-dependent mixture of Dy^{top} and $Dy^{br\text{-}x}$ contributions. The $Dy^{br\text{-}y}$ atoms are inaccessible to XMCD in our experimental geometry because their magnetic moment always maintains a perpendicular orientation with respect to the external magnetic field. They manifest themselves only in the XAS and XLD spectra.

From the energy schemes in Figure 5 we also infer a longer spin lifetime for Dy^{br} as compared to Dy^{top}. The Dy^{br} energy level diagram closely resembles the parabolic schemes reported for DyO complexes.[20–22] In all these cases, given the almost pure states, spin reversal takes place via the top of the barrier. On the contrary, the inverted double well shaped energy scheme of Dy^{top} favors spin reversal via thermal-activated QTM paths.

Experimentally we observe very similar magnetization hysteresis at normal and grazing incidence where only Dy^{top} or both Dy^{top} and Dy^{br} contribute, respectively, revealing that the observed hysteretic magnetic behavior is photon-flux limited.[1,7,23] This is well exemplified in Figure 1f where τ decreases by increasing the photon flux. The $\tau = 310 \pm 50$ s reported for the lowest flux has then to be considered as a lower limit for the intrinsic spin lifetimes. We note that de-magnetization induced by spin scattering with secondary electrons generated by the X-ray beam is particularly severe in the case of BaO compared with similar systems, such as Ho/MgO[1] or $Dy/SrTiO_3$,[23]

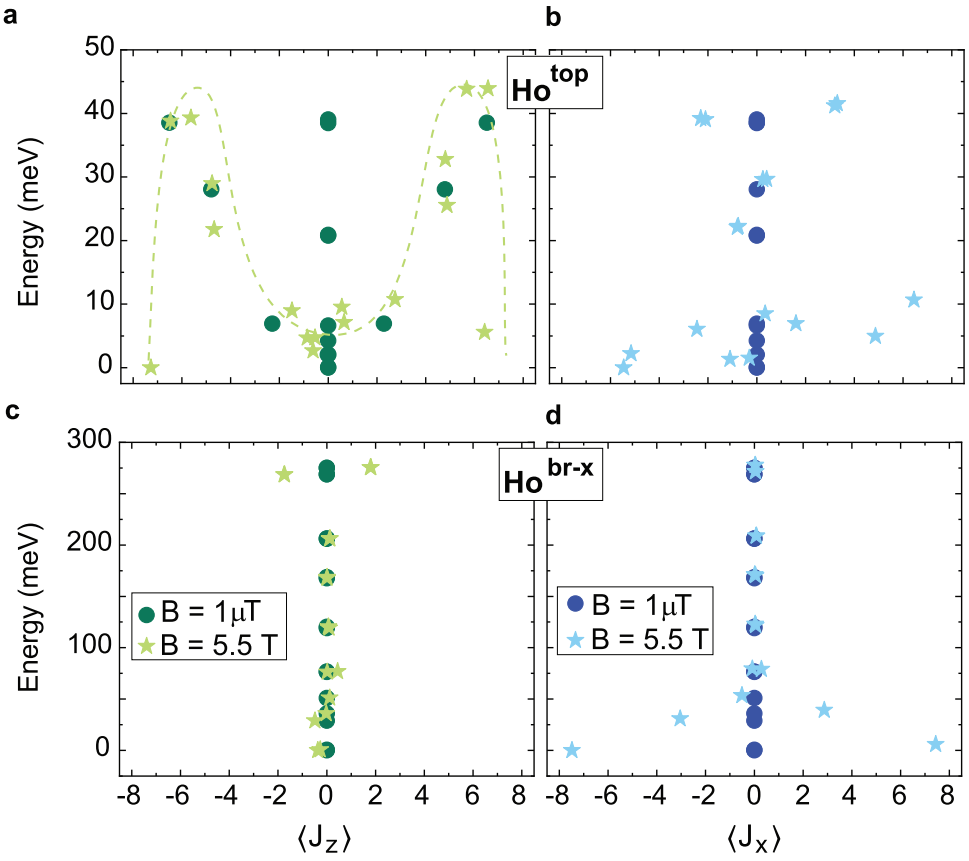

Figure 6. Quantum level scheme of the ground J multiplet for (a,b) Ho^{top} and (c,d) $Ho^{br\text{-}x}$ atoms on BaO in small (1 μT) and high (5.5 T) magnetic field applied along z and x axes. The dashed line illustrate the energy barriers separating states with opposite spins.

where similar photon fluxes limited τ to about 1000 s. This is a consequence of the X-ray absorption coefficient at the Dy M_5 edge that for BaO (3.3 μm^{-1}) is more than twice the value for MgO at the Ho M_5 edge (1.5 μm^{-1}) and ≈3 times the value for $SrTiO_3$ (1.1 μm^{-1}).[41] The strong photon induced de-magnetization makes it experimentally difficult to systematically investigate the flux dependence of the spin lifetime and, thus, to evaluate its intrinsic value.

In the Ho case, good agreement with the data requires a slight increase of the effective charges of the Ho-O bond in the top-O site by about 15%. The quantum level schemes for Ho^{top} and $Ho^{br\text{-}x}$ projected along easy and hard axes are shown

Table 2. Wavefunction composition of the ground state doublet. Ln^{top} states are expressed in terms of J_z; $Ln^{br\text{-}x}$ and $Ln^{br\text{-}y}$ in terms of J_x and J_y, respectively.

Dy																
J_i	$-\frac{15}{2}$	$-\frac{13}{2}$	$-\frac{11}{2}$	$-\frac{9}{2}$	$-\frac{7}{2}$	$-\frac{5}{2}$	$-\frac{3}{2}$	$-\frac{1}{2}$	$\frac{1}{2}$	$\frac{3}{2}$	$\frac{5}{2}$	$\frac{7}{2}$	$\frac{9}{2}$	$\frac{11}{2}$	$\frac{13}{2}$	$\frac{15}{2}$
$-\psi^{top}$	0.655	0	0	0	0.195	0	0	0	0.726	0	0	0	0.064	0	0	0
$+\psi^{top}$	0	0	0	0.064	0	0	0	0.726	0	0	0	0.195	0	0	0	0.655
$-\psi^{br}$	0.963	0	0.221	0	0.057	0	0.016	0	0.006	0	0.003	0	0.001	0	0.001	0
$+\psi^{br}$	0	0.001	0	0.001	0	0.003	0	0.006	0	0.016	0	0.057	0	0.221	0	0.963

Ho																	
J_i	−8	−7	−6	−5	−4	−3	−2	−1	0	1	2	3	4	5	6	7	8
$-\psi^{top}$	0.624	0	0	0	0.316	0	0	0	0.138	0	0	0	0.316	0	0	0	0.624
$+\psi^{top}$	0.624	0	0	0	0.316	0	0	0	0.138	0	0	0	0.316	0	0	0	0.624
$-\psi^{br}$	0.629	0	0.276	0	0.120	0	0.075	0	0.063	0	0.075	0	0.120	0	0.276	0	0.629
$+\psi^{br}$	0.629	0	0.276	0	0.120	0	0.075	0	0.063	0	0.075	0	0.120	0	0.276	0	0.629

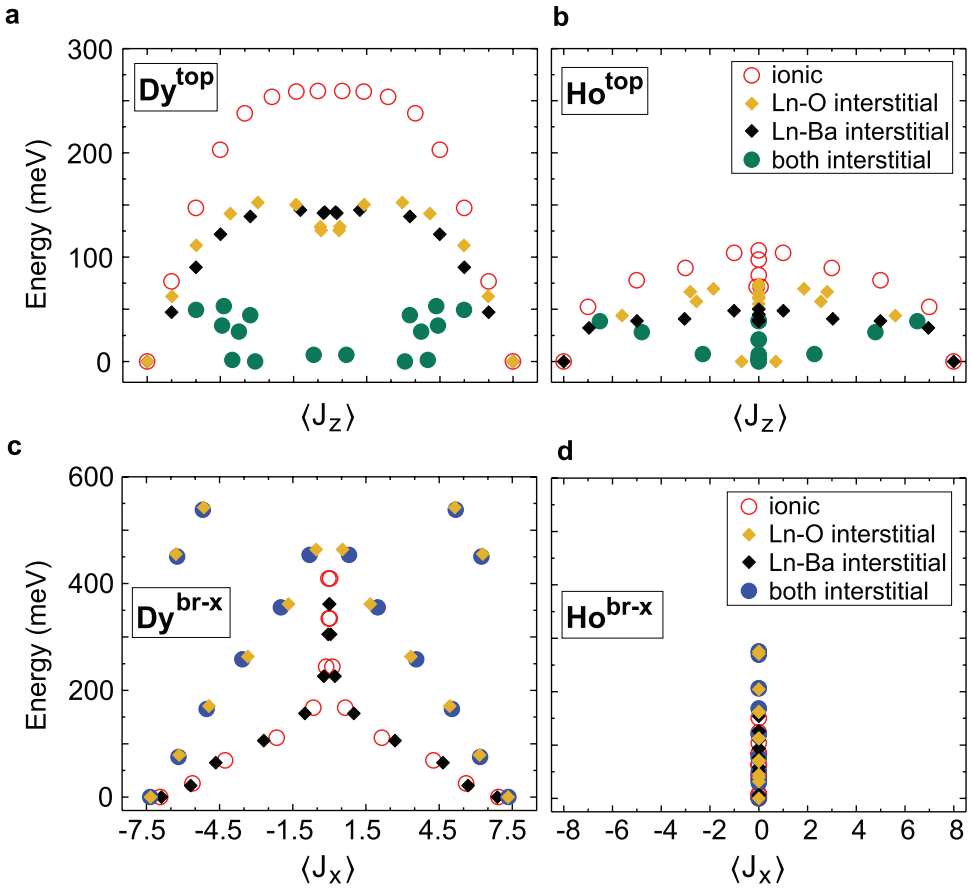

Figure 7. Quantum level schemes of the ground J multiplet for a,c) Dy and b,d) Ho adsorbed on both top-O and bridge sites on BaO generated by different sets of point charges. The schemes are calculated along the respective easy axes, in a magnetic field of 1 µT. Data marked with green and blue dots are the same as in Figures 5 and 6.

in Figure 6. The Ho^{top} and Ho^{br} ground-state wavefunctions are given in Table 2. The Ho $4f^{10}$ electronic configuration leads to a $J = 8$ non-Kramers lowest energy multiplet. The ground state doublets of both Ho^{top} and Ho^{br} species are strongly mixed by the CF. This mixing, surviving also in presence of magnetic field, favors QTM and explains the absence of hysteresis in the measured magnetization curves.

Comparing the magnetic behavior of Ho and Dy adatoms on BaO with the one previously reported on MgO suggests some general rules in the quest for the optimum combination of Ln, adsorption site, and supporting alkaline earth oxide leading to long spin relaxation time. Dy is in general a better candidate than Ho. For the same adsorption site and substrate, Dy $4f^9$ shows higher energy barriers than Ho $4f^{10}$. In addition, level mixing and thus QTM is reduced for the Kramers Dy compared to the non-Kramers Ho. Looking for the ideal Ln adsorption site, we observe that top-O on BaO, under the assumption of an ionic CF, i.e., Bader charges centered on the atom positions, would produce quantum level schemes (see **Figure 7**a,b) qualitatively identical to the ones reported for MgO.[1,3–5] However, Ln adsorption on BaO, alkaline earth oxide characterized by a smaller lattice energy compared to MgO, produces a local surface distortion involving both the closest anions and cations. This distortion strongly affects the CF by introducing negative (positive) interstitial charges along the Ln-O (Ln-Ba) direction. Figure 7a,b shows that both negative and positive interstitial charges have a similar detrimental effect reducing the barrier height by one half. Their combined effect transforms the shape of the quantum level scheme from almost parabolic to an inverted double well with strong mixing between states on the opposite side of the barrier. Curiously, at bridge sites, local surface distortions turn out to be advantageous. For both elements we observe higher energy barriers on BaO than on MgO and, for Dy, an increased level purity (see Figure 7c,d). The deviation from the ideal half-integer J_x values stems from mixing of states on the same side of the energy barrier (see Table 2); thus, Dy^{br} on BaO is characterized by a quantum level scheme prone to promote very long spin lifetimes.

3. Conclusion

In conclusion, we have investigated the electronic and magnetic properties of Dy and Ho atoms adsorbed on BaO thin films grown on Pt(100). Both Ln species are found in their bulk electronic configuration, i.e., $4f^9$ and $4f^{10}$ for Dy and Ho, respectively. Dy adatoms show slow magnetic relaxation for magnetic fields up to ≈3.5 T; the measured spin lifetime of ≈300 s represents

a lower limit for the intrinsic spin lifetime. On the contrary, Ho adatoms show magnetic relaxation faster than our experimental resolution of ≈10 s. A comparison of the experimental data with first-principles and multiplet calculations allows us to rationalize our observations and the differences with respect to the same two elements adsorbed on MgO. On BaO, Ln adatom adsorption produces a strong surface distortion affecting the closest O and Ba atoms, determining the CF acting on the Ln adatom. At the bridge site, Dy is characterized by an almost ideal axial CF creating an easy axis along the O-Dy-O direction and a barrier height exceeding 0.45 eV. On the contrary, Ho is affected by strong state mixing induced by the C_{2v} symmetric CF. Top-O species are characterized by an inverted double well shaped energy diagram. The C_{4v} symmetric CF causes efficient QTM for the $J = 8$ Ho adatom, while a higher spin stability is observed for the Kramers Dy. Differently, on MgO, characterized by a larger lattice energy compared to BaO, the local surface distortion affects only the closest O atoms. This results in an almost axial CF for the top-O adsorption site, while adatoms on bridge sites behave similarly to the BaO case. Our work provides criteria for selecting those combinations of Ln, adsorption site, and supporting alkaline earth oxide that achieves the longest spin relaxation times.

4. Experimental Section

The Pt(100) single crystal was prepared in situ in the preparation chamber of the EPFL/PSI X-Treme beamline at the Swiss Light Source by repeated cycles of Ar^+ sputtering and annealing at a temperature $T \approx 1170$ K. The BaO(100) thin films were grown in situ by evaporation of Ba (Mateck, 99.3% purity) from an effusion cell in an O_2 partial pressure of 1×10^{-6} mbar onto a substrate held at 670 K, with subsequent annealing for 30 min at 920 K in UHV ($p \approx 10^{-8}$ mbar). The stoichiometry, crystallinity, and thickness of BaO films were characterized by low energy electron diffraction (LEED), XAS and XLD (see Supporting Information). The BaO thickness was calibrated by the Ba M_5 XAS peak intensity. For this, one reference sample with a BaO coverage of ≈0.7 ML was grown as determined by scanning tunneling microscopy performed in the laboratory at EPFL.

Dy and Ho adatoms were deposited from high purity rods (99.9%) at $T < 5$ K and $p \approx 3 \times 10^{-11}$ mbar, using an e-beam evaporator installed on the same cryostat used to perform the XAS measurements. The Ln coverage Θ_{Ln} is expressed in ML where one ML corresponds to one Ln atom per BaO(100) surface unit cell, or equivalently to a surface density of 6.5 atoms nm^{-2}.

The X-ray absorption experiments were performed at the EPFL/PSI X-Treme beamline at the Swiss Light Source.[28] The measurements were carried out in the total-electron-yield mode at $T \approx 2.5$ K. The XAS, XMCD, and XLD correspond to $(\sigma^+ + \sigma^-)$, $(\sigma^+ - \sigma^-)$, and $(\sigma^v - \sigma^h)$ respectively, where σ^+, σ^- are the absorption of right-handed and left-handed circularly polarized X-rays, and σ^h, σ^v the absorption of horizontal and vertical linearly polarized X-rays. The background signals were recorded in the energy range defined by the Ln $M_{4,5}$ edges on clean BaO films prior to adatom deposition and subsequently subtracted from the corresponding Ln spectra. All spectra have been normalized to the pre-edge signal intensity and to the integral over the Ln M_5 edge absorption signal.

DFT calculations were carried out by employing the augmented-plane wave+local orbital method as implemented in the Wien2K code.[42] The generalized-gradient approximation (GGA)[43] of the exchange and correlation functional was considered for the structural characterization, while the electronic structure analysis was obtained by using an on-site version of the hybrid B3LYP functional.[30,44] In the authors' experience, this functional is better suited (as compared to the more standard +*U* methods) to achieve the correct 4*f* occupation in the ground state, which is a key issue in elements such as Dy that can attain different valencies. Moreover it bypasses the need of the *U* parameter's choice which always involves a certain degree of arbitrariness, particularly when results for different Ln species are compared. Calculations were performed without spin-orbit interaction. The electronic occupation on the Ln atoms and the analysis of the adatom/substrate charge transfer is performed both analyzing the orbital occupations integrated within a sphere centered at the Ln nuclei as well as the quantum theory of atoms in molecules proposed by Bader.[45] Simulation cells were constructed by considering a 2×2 in-plane cell periodicity, and a 6 ML thick substrate slab. Vacuum space between the slabs replica was included to avoid spurious slab-slab interaction. The coordinates of the Ln adatoms and of the upper two substrate layer atoms were relaxed till residual forces were less than 1 meV $a.u.^{-1}$. Further detail on the simulation cells can be found in the Supporting Information.

The multiX code was used to perform the multiplet simulations.[33] The Slater–Condon integrals were scaled to 75%, core electrons spin-orbit coupling to 97%, valence electrons spin-orbit coupling to 85%. A core–hole lifetime lorentzian broadening of 0.6 eV was used. The point charges can be found in the Supporting Information.

Supporting Information

Supporting Information is available from the Wiley Online Library or from the author.

Acknowledgements

The authors acknowledge funding from the Swiss National Science Foundation (grants number 200021_175941, 200020_176932, 200020_204426). Computation time at the CINECA supercomputing center is gratefully acknowledged.

Open access funding provided by Ecole Polytechnique Fédérale de Lausanne.

Conflict of Interest

The authors declare no conflict of interest.

Data Availability Statement

The data that support the findings of this study are available from the corresponding author upon reasonable request.

Keywords

alkaline earth oxides, density functional theory, lanthanides, magnetic relaxation, multiplet calculations, single atom magnets, X-ray magnetic circular dichroism

Received: November 29, 2022
Revised: January 10, 2023
Published online:

[1] F. Donati, S. Rusponi, S. Stepanow, C. Wäckerlin, A. Singha, L. Persichetti, R. Baltic, K. Diller, F. Patthey, E. Fernandes, J. Dreiser, Ž. Šljivančanin, K. Kummer, C. Nistor, P. Gambardella, H. Brune, *Science* **2016**, *352*, 318.

[2] F. D. Natterer, K. Yang, W. Paul, P. Willke, T. Choi, T. Greber, A. J. Heinrich, C. P. Lutz, *Nature* **2017**, *543*, 226.
[3] A. Singha, P. Willke, T. Bilgeri, X. Zhang, H. Brune, F. Donati, A. J. Heinrich, T. Choi, *Nat. Commun.* **2021**, *12*, 4179.
[4] F. D. Natterer, F. Donati, F. Patthey, H. Brune, *Phys. Rev. Lett.* **2018**, *121*, 027201.
[5] F. Donati, M. Pivetta, C. Wolf, A. Singha, C. Wäckerlin, R. Baltic, E. Fernandes, J.-G. de Groot, S. L. Ahmed, L. Persichetti, C. Nistor, J. Dreiser, A. Barla, P. Gambardella, H. Brune, S. Rusponi, *Nano Lett.* **2021**, *21*, 8266.
[6] P. R. Forrester, F. Patthey, E. Fernandes, D. P. Sblendorio, H. Brune, F. D. Natterer, *Phys. Rev. B* **2019**, *100*, 180405.
[7] R. Baltic, M. Pivetta, F. Donati, C. Wäckerlin, A. Singha, J. Dreiser, S. Rusponi, H. Brune, *Nano Lett.* **2016**, *16*, 7610.
[8] C. A. P. Goodwin, F. Ortu, D. Reta, N. F. Chilton, D. P. Mills, *Nature* **2017**, *548*, 439.
[9] F.-S. Guo, B. M. Day, Y.-C. Chen, M.-L. Tong, A. Mansikkamäki, R. A. Layfield, *Science* **2018**, *362*, 1400.
[10] F.-S. Guo, B. M. Day, Y.-C. Chen, M.-L. Tong, A. Mansikkamäki, R. A. Layfield, *Angew. Chem. Int. Ed.* **2017**, *56*, 11445.
[11] R. Westerström, J. Dreiser, C. Piamonteze, M. Muntwiler, S. Weyeneth, H. Brune, S. Rusponi, F. Nolting, A. Popov, S. Yang, L. Dunsch, T. Greber, *J. Am. Chem. Soc.* **2012**, *134*, 9840.
[12] C. Wäckerlin, F. Donati, A. Singha, R. Baltic, S. Rusponi, K. Diller, F. Patthey, M. Pivetta, Y. Lan, S. Klyatskaya, M. Ruben, H. Brune, J. Dreiser, *Adv. Mater.* **2016**, *28*, 5195.
[13] K. S. Pedersen, A.-M. Ariciu, S. McAdams, H. Weihe, J. Bendix, F. Tuna, S. Piligkos, *J. Am. Chem. Soc.* **2016**, *138*, 5801.
[14] E. Moreno-Pineda, C. Godfrin, F. Balestro, W. Wernsdorfer, M. Ruben, *Chem. Soc. Rev.* **2018**, *47*, 501.
[15] S. Thiele, F. Balestro, R. Ballou, S. Klyatskaya, M. Ruben, W. Wernsdorfer, *Science* **2014**, *344*, 1135.
[16] N. Ishikawa, M. Sugita, T. Ishikawa, S.-y. Koshihara, Y. Kaizu, *J. Am. Chem. Soc.* **2003**, *125*, 8694.
[17] J. Dreiser, *J. Phys.: Condens. Matter* **2015**, *27*, 183203.
[18] A. K. Bar, P. Kalita, M. K. Singh, G. Rajaraman, V. Chandrasekhar, *Coord. Chem. Rev.* **2018**, *367*, 163.
[19] K. Diller, A. Singha, M. Pivetta, C. Wäckerlin, R. Hellwig, A. Verdini, A. Cossaro, L. Floreano, E. Vélez-Fort, J. Dreiser, S. Rusponi, H. Brune, *RSC Adv.* **2019**, *9*, 34421.
[20] L. Ungur, L. F. Chibotaru, *Phys. Chem. Chem. Phys.* **2011**, *13*, 20086.
[21] L. Ungur, L. F. Chibotaru, *Inorg. Chem.* **2016**, *55*, 10043.
[22] W. Zhang, A. Muhtadi, N. Iwahara, L. Ungur, L. F. Chibotaru, *Angew. Chem. Int. Ed.* **2020**, *59*, 12720.
[23] V. Bellini, S. Rusponi, J. Kolorenč, S. K. Mahatha, M. A. Valbuena, L. Persichetti, M. Pivetta, B. V. Sorokin, D. Merk, S. Reynaud, D. Sblendorio, S. Stepanow, C. Nistor, P. Gargiani, D. Betto, A. Mugarza, P. Gambardella, H. Brune, C. Carbone, A. Barla, *ACS Nano* **2022**, *16*, 11182.
[24] M. F. C. Ladd, W. H. Lee, *Acta Crystallogr.* **1960**, *13*, 959.
[25] S. Cantor, *J. Chem. Phys.* **1973**, *59*, 5189.
[26] G. Pacchioni, C. Sousa, F. Illas, F. Parmigiani, P. S. Bagus, *Phys. Rev. B* **1993**, *48*, 11573.
[27] C. Di Valentin, R. Ferullo, R. Binda, G. Pacchioni, *Surf. Sci.* **2006**, *600*, 1147.
[28] C. Piamonteze, U. Flechsig, S. Rusponi, J. Dreiser, J. Heidler, M. Schmidt, R. Wetter, M. Calvi, T. Schmidt, H. Pruchova, J. Krempasky, C. Quitmann, H. Brune, F. Nolting, *J. Synchrotron Rad.* **2012**, *19*, 661.
[29] A. Singha, R. Baltic, F. Donati, C. Wäckerlin, J. Dreiser, L. Persichetti, S. Stepanow, P. Gambardella, S. Rusponi, H. Brune, *Phys. Rev. B* **2017**, *96*, 224418.
[30] A. D. Becke, *J. Chem. Phys.* **1993**, *98*, 5648.
[31] S. Tosoni, G. Pacchioni, *Phys. Chem. Chem. Phys.* **2022**, *24*, 15891.
[32] E. Fernandes, F. Donati, F. Patthey, S. Stavrić, Ž. Šljivančanin, H. Brune, *Phys. Rev. B* **2017**, *96*, 045419.
[33] A. Uldry, F. Vernay, B. Delley, *Phys. Rev. B* **2012**, *85*, 125133.
[34] C. K. Jorgensen, R. Pappalardo, H. Schmidtke, *J. Chem. Phys.* **1963**, *39*, 1422.
[35] R. E. Watson, A. J. Freeman, *Phys. Rev.* **1967**, *156*, 251.
[36] H. Bethe, *Ann. Phys.* **1929**, *395*, 133.
[37] Z. Zolnierek, *J. Phys. Chem. Solids* **1984**, *45*, 523.
[38] P. Porcher, M. Couto Dos Santos, O. Malta, *Phys. Chem. Chem. Phys.* **1999**, *1*, 397.
[39] J. J. Baldoví, S. Cardona-Serra, J. M. Clemente-Juan, E. Coronado, A. Gaita-Ariño, A. Palii, *Inorg. Chem.* **2012**, *51*, 12565.
[40] S.-D. Jiang, S.-X. Qin, *Inorg. Chem. Front.* **2015**, *2*, 613.
[41] B. L. Henke, E. M. Gullikson, J. C. Davis, *At. Data Nucl. Data Tables* **1993**, *54*, 181.
[42] P. Blaha, K. Schwarz, G. K. H. Madsen, D. Kvasnicka, J. Luitz, *WIEN2k, an Augmented Plane Wave + Local Orbitals Program for Calculating Crystal Properties*, (Ed: K. Schwarz), Techn. Universität, Wien, Austria **2001**.
[43] J. P. Perdew, K. Burke, M. Ernzerhof, *Phys. Rev. Lett.* **1996**, *77*, 3865.
[44] F. Tran, P. Blaha, K. Schwarz, P. Novák, *Phys. Rev. B* **2006**, *74*, 155108.
[45] R. F. W. Bader, R. F. Bader, *Atoms in Molecules: A Quantum Theory, International Series of Monographs on Chemistry*, Clarendon Press, Oxford, UK **1990**.

ADVANCED FUNCTIONAL MATERIALS

Supporting Information

for *Adv. Funct. Mater.,* DOI: 10.1002/adfm.202213951

The Impact of Lattice Distortions on the Magnetic Stability of Single Atoms: Dy and Ho on BaO(100)

*Boris V. Sorokin, Marina Pivetta, Valerio Bellini, Darius Merk, Sébastien Reynaud, Alessandro Barla, Harald Brune, and Stefano Rusponi**

Supporting information for "The Impact of Lattice Distortions on the Magnetic Stability of Single Atoms: Dy and Ho on BaO(100)"

Boris V. Sorokin[1], Marina Pivetta[1], Darius Merk[1], Sébastien Reynaud[1], Valerio Bellini[2], Alessandro Barla[3], Harald Brune[1], and Stefano Rusponi[1]

[1]Institute of Physics, Ecole Polytechnique Fédérale de Lausanne (EPFL), Station 3, CH-1015 Lausanne, Switzerland
[2]S3-Istituto di Nanoscienze-CNR, Via Campi 213/A, I-41125 Modena, Italy
[3]Istituto di Struttura della Materia (ISM), Consiglio Nazionale delle Ricerche (CNR), I-34149 Trieste, Italy

BaO thin film characterization

The low energy electron diffraction (LEED) pattern of the clean Pt(100) surface is shown in Figure S1(a). The image exhibits a typical Pt(100)-hex surface reconstruction (also called Pt(100)-(5×20)).[1] The LEED pattern of 6 ML thick BaO(100) film grown on Pt(100) is shown in Figure S1(b) and corresponds to a Pt(100)-c(2×2) structure.[2,3] The pattern is generated by a BaO(100)-(1×1) rotated by 45° with respect to Pt(100). This orientation is favored as the 45° rotation results in a perfect lattice match between BaO (5.54 Å) and Pt(100) (3.92 Å), see Figure S1(c).

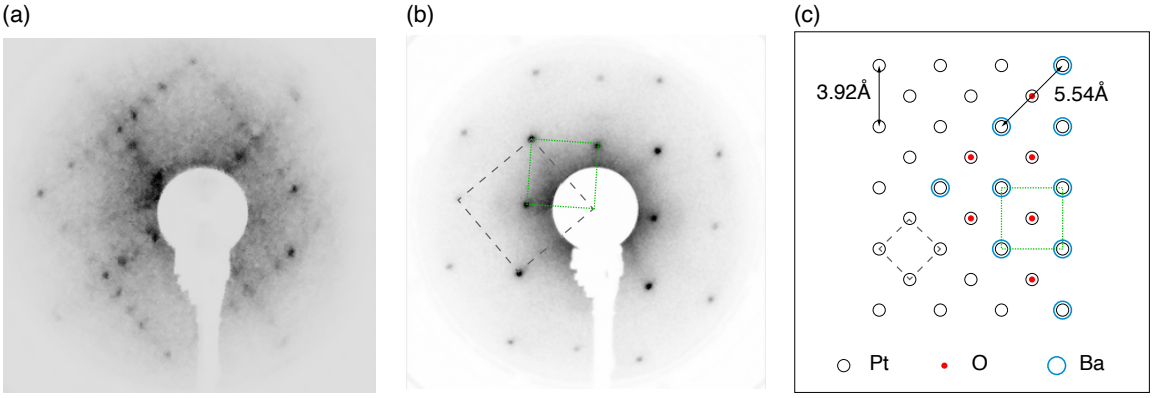

Figure S1: LEED images of (a) Pt(100) single crystal and (b) BaO(100) thin film (6 ML) grown on Pt(100). Both patterns have been acquired with an electron beam energy of 80 eV. (c) Real space sketch of the arrangement of Ba and O atoms on Pt(100).

The horizontal direction in Figure S1 is approximately parallel to the x axis (as defined in the main text). Thus, we infer an angle of about 5° between the BaO[010] crystallographic direction and the x axis. No influence of this misalignment on the results of the multiplet simulations was found. Hence, we neglected this small misalignment and considered the [010] direction parallel to x axis in our data analysis.

The XAS acquired at the O K-edge with vertical and horizontal linear polarized X-rays, as well as the corresponding XLD spectrum, are shown in Figure S2. The well defined multiplet structure indicates that O is found in a well oriented crystalline structure.

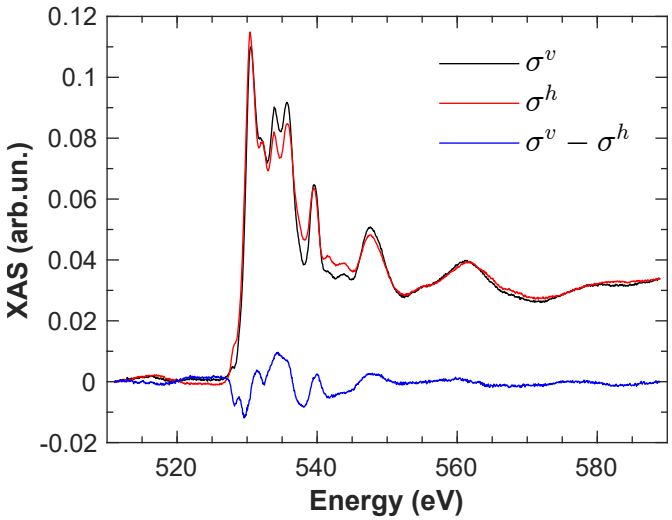

Figure S2: O K-edge absorption of vertically (σ^v, black line) and horizontally (σ^h, red line) polarized X-rays together with XLD (σ^v-σ^h, blue line).

DFT calculations: simulation cell

Since we verified experimentally that the electronic configuration of Dy and Ho does not change by increasing the thickness (up to 8 ML) of BaO on Pt, in our DFT calculations the BaO(100) substrate was simulated by a 6 ML thick slab, without including the Pt substrate, as depicted in Figure S3. Vacuum space was added in the direction normal to the surface in order to avoid spurious interaction between the slabs replica. In order to describe the case of isolated Ln adatoms, a 2×2 in-plane periodicity was assumed. Similarly, for MgO, we removed the Ag substrate, and considered the same simulation cells as for BaO. The experimental BaO and MgO lattice constants of $a^{latt}_{BaO} = 5.54$Å and $a^{latt}_{MgO} = 4.21$Å were used. The coordinates of the Ln adatoms and of the upper two substrate layer atoms were relaxed till residual forces were less than 1 meV/a.u..

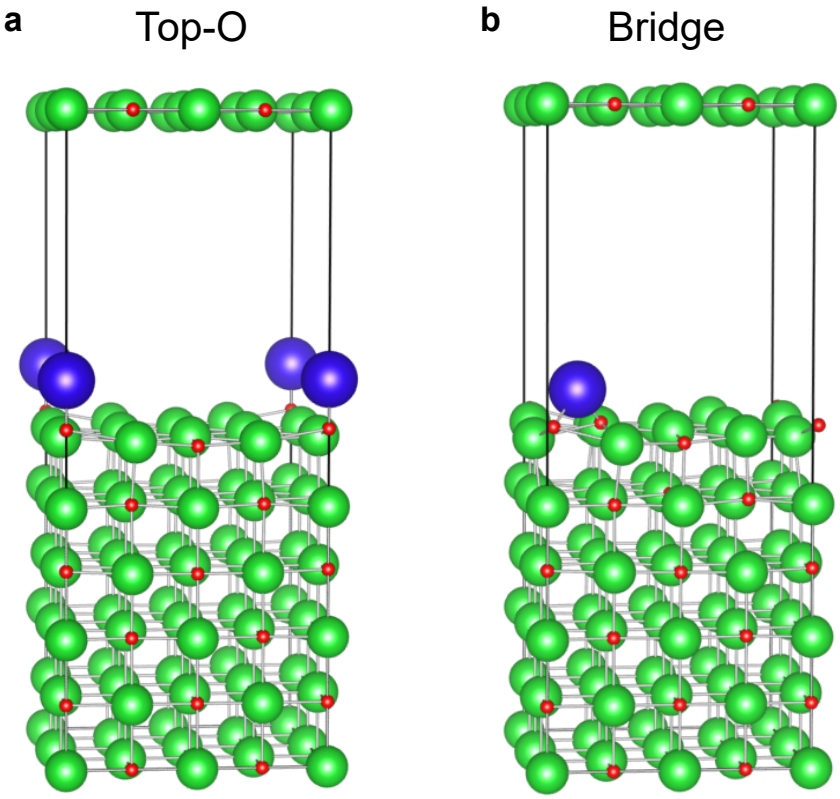

Figure S3: Simulation cells for Ln adatoms on the BaO (or MgO) surface, for the (a) top-O and (b) bridge adsorption sites. O, Ba(Mg) and Dy(Ho) atoms are depicted with small red, medium green and large blue spheres, respectively.

DFT calculations: valence orbital occupations

We present here the electronic occupation, as calculated by the Wien2K code, of each valence orbital, i.e. s, p, d and f, for the Dy and Ho adatoms on BaO. In the LAPW+lo basis set employed in Wien2K, the space is intrinsically divided in spheres centered at each atom nuclei (with so-called muffin-tin radii) and an interstitial region (whatever is left outside such spheres). The occupations are obtained by integrating the electronic charge density, for each quantum number l, inside the muffin-tin sphere centered at the atom of interest. When semi-core states are considered in the valence region (for technical reasons), the electronic occupation is the sum of the occupation of orbitals with the same l but different principal quantum number n. For instance, in the case of Dy and Ho elements, $5s$ and $5p$ semicore states are included in the valence region so that s and p occupations are relative to $5s + 6s$ and $5p + 6p$ orbitals, respectively.

Tables S1 and S2 show the electronic occupations of the s, p, d, and f valence shells for Dy and Ho adatoms on top-O and bridge adsorption sites on BaO(100) and as isolated atoms. In case of spatially extended orbitals, such as $6s$ and $6p$ orbitals, the occupation numbers are extremely underestimated, and vary sensibly as a function of the chosen muffin-tin integration radius. For example, in the case of the isolated atoms, only 3 of the expected 4 s electrons are counted, even increasing the integration radius to a large value such as 4.0 a.u.. On the contrary, f (and to a lesser extent d) orbitals are much more localized in space, and their occupations are integrated with higher accuracy. This can be seen in the case of the Dy isolated atoms in Table S1, with the values in parenthesis giving the occupations that are instantaneously attained in the valence *spdf* shells during the self-consistency cycle, when electrons, before reaching the self-consistent ground state, jump from the $4f$ to the $5d$ shell. It can be seen that only 70% of the $5d$ occupation is obtained even for a muffin-tin radius of 4.0 a.u.. These reference values represent the charge that should be found by integration, within a certain muffin-tin sphere, in the $5s + 6s$ and $5d$ orbitals when they nominally host 4 and 1 electrons, respectively. Note that, for isolated atoms, the valence orbitals are more extended in space as compared to the adatoms, since there is no electrostatic repulsion from neighboring atoms; thus, the occupations calculated for the isolated atoms should be considered as a lower limit.

Table S1: Calculated electronic occupations of $5s+6s$ (n_s), $5p+6p$ (n_p), $5d$ (n_d), and $4f$ (n_f) shells for Dy top-O and bridge on BaO, and Dy isolated atom; different Dy muffin-tin radii r_{MT} are considered. See text for more details.

Dy top-O on BaO				
r_{MT}(Dy) (a.u.)	n_s (e^-)	n_p (e^-)	n_d (e^-)	n_f (e^-)
2.4	2.11	5.56	0.30	9.56
2.8	2.28	5.88	0.41	9.75
Dy bridge on BaO				
r_{MT}(Dy) (a.u.)	n_s (e^-)	n_p (e^-)	n_d (e^-)	n_f (e^-)
2.4	2.13	5.66	0.60	8.96
2.8	2.31	5.99	0.96	9.11
Dy isolated atom				
r_{MT}(Dy) (a.u.)	n_s (e^-)	n_p (e^-)	n_d (e^-)	n_f (e^-)
2.4	2.13	5.50	0.00	9.74
	(2.13)	(5.50)	(0.36)	(8.85)
2.8	2.33	5.80	0.00	9.86
	(2.33)	(5.80)	(0.44)	(8.90)
4.0	3.01	5.99	0.00	9.97
	(3.01)	(5.99)	(0.68)	(8.98)

Although absolute values are not reliable, some understanding can be achieved by comparing the results of the interacting systems (Ln adatom+substrate) with the ones of isolated Ln atoms. We observe a similar trend in the occupation of the $6s$ orbital for the Dy adatoms (Table S1) and the

Table S2: Calculated electronic occupations of $5s + 6s$ (n_s), $5p + 6p$ (n_p), $5d$ (n_d), and $4f$ (n_f) shells for Ho top-O and bridge on BaO, and Ho isolated atom; for the latter, different Ho muffin-tin radii r_{MT} are considered.

Ho top-O on BaO

r_{MT}(Ho) (a.u.)	n_s (e^-)	n_p (e^-)	n_d (e^-)	n_f (e^-)
2.4	2.16	5.66	0.61	9.93

Ho bridge on BaO

r_{MT}(Ho) (a.u.)	n_s (e^-)	n_p (e^-)	n_d (e^-)	n_f (e^-)
2.4	2.15	5.69	0.59	9.94

Ho isolated atom

r_{MT}(Ho) (a.u.)	n_s (e^-)	n_p (e^-)	n_d (e^-)	n_f (e^-)
2.4	2.15	5.56	0.00	10.76
4.0	3.04	5.99	0.00	10.98

isolated Dy atom, with increasing muffin tin spheres from 2.4 to 2.8 a.u., meaning that the $6s$ orbital has an important occupation for the Dy adatoms, close to the isolated atom value of $6s^2$. Moreover, the combined occupation of the $5d$ and $4f$ orbitals sums up to around 10 electrons for Dy. Instead, the occupation of the p orbitals is compatible with the presence of the $5p$ semi-core state, with only a minor contribution from the $6p$ orbital. Unfortunately, we could not increase the muffin tin radius for the adatoms to more than 2.8 a.u., since the sphere would overlap with the muffin tin spheres of the neighboring O substrate atoms. Similar behavior is found for Ho (see Table S2).

In virtue of this analysis, we conclude that when trivalent states are found, roughly one electron moves from the $4f$ to the $5d$ orbitals, and in all cases the $6s$ shell continues to host most of the charge present in the free atom case, meaning that the charge transfer from the Dy (Ho) adatoms to the substrate is very limited. This is in agreement with the Bader analysis that shows that only a fraction of an electron is transferred outside the adatom regions.

DFT calculations: Bader charges and atomic coordinates

Table S3: Distance from the Ln adatom, Bader charges and atomic coordinates for the atoms composing the first four coordination shells around Ln, for a Dy adatom on the top-O adsorption site on BaO.

Atom	Shell	Distance (in Å)	Bader Charge (in e^-)	Cartesian Coordinates x (Å)	y (Å)	z (Å)
Dy	-	-	+0.20	0.000	0.000	0.000
O	1st	2.077	-1.36	0.000	0.000	-2.077
Ba	2nd	3.900	+1.36	0.000	2.907	-2.601
				2.907	0.000	-2.601
				0.000	-2.907	-2.601
				-2.907	0.000	-2.601
O	3rd	4.832	-1.38	2.783	2.783	-2.804
				2.783	-2.783	-2.804
				-2.783	2.783	-2.804
				-2.783	-2.783	-2.804
Ba	4th	5.372	+1.38	0.000	0.000	-5.372

Table S4: Distance from the Ln adatom, Bader charges and atomic coordinates for the atoms composing the first three coordination shells around the Ln, for a Dy adatom on the bridge adsorption site on BaO.

Atom	Shell	Distance (in Å)	Bader Charge (in e^-)	Cartesian Coordinates x (Å)	y (Å)	z (Å)
Dy	-	-	+0.57	0.000	0.000	0.000
O	1st	2.148	-1.39	-1.100	-1.100	-1.481
				1.100	1.100	-1.481
Ba	2nd	3.209	+1.30	-1.675	1.675	-2.165
				1.675	-1.675	-2.165
Ba	3rd	4.798	+1.40	-1.369	-4.193	-1.888
				-4.193	-1.369	-1.888
				4.193	1.369	-1.888
				1.369	4.193	-1.888

Table S5: Distance from the Ln adatom, Bader charges and atomic coordinates for the atoms composing the first four coordination shells around the Ln, for Ho adatom on top-O adsorption site on BaO.

Atom	Shell	Distance (in Å)	Bader Charge (in e^-)	Cartesian Coordinates x (Å)	y (Å)	z (Å)
Ho	-	-	+0.14	0.000	0.000	0.000
O	1st	2.085	-1.34	0.000	0.000	-2.085
Ba	2nd	3.884	+1.36	0.000	2.899	-2.585
				2.899	0.000	-2.585
				0.000	-2.899	-2.585
				-2.899	0.000	-2.585
O	3rd	4.822	-1.38	2.782	2.782	-2.787
				2.782	-2.782	-2.787
				-2.782	2.782	-2.787
				-2.782	-2.782	-2.787
Ba	4th	5.356	+1.38	0.000	0.000	-5.356

Table S6: Distance from the Ln adatom, Bader charges and atomic coordinates for the atoms composing the first three coordination shells around the Ln, for a Ho adatom on the bridge adsorption site on BaO.

Atom	Shell	Distance (in Å)	Bader Charge (in e^-)	Cartesian Coordinates x (Å)	y (Å)	z (Å)
Ho	-	-	+0.62	0.000	0.000	0.000
O	1st	2.168	-1.38	-1.099	-1.099	-1.511
				1.099	1.099	-1.511
Ba	2nd	3.191	+1.30	-1.672	1.672	-2.142
				1.672	-1.672	-2.142
Ba	3rd	4.781	1.39	-1.363	-4.184	-1.868
				-4.184	-1.363	-1.868
				4.184	1.363	-1.868
				1.363	4.184	-1.868

Table S7: Distance from the Ln adatom, Bader charges and atomic coordinates for the atoms composing the first four coordination shells around the Ln, for a Dy adatom on the top-O adsorption site on MgO.

Atom	Shell	Distance (in Å)	Bader Charge (in e^-)	Cartesian Coordinates x (Å)	y (Å)	z (Å)
Dy	-	-	+0.20	0.000	0.000	0.000
O	1st	2.274	-1.69	0.000	0.000	-2.274
Mg	2nd	3.407	+1.68	0.000	2.172	-2.625
				2.172	0.000	-2.625
				0.000	-2.172	-2.625
				-2.172	0.000	-2.625
O	3rd	3.964	-1.72	2.106	2.106	-2.616
				2.106	-2.106	-2.616
				-2.106	2.106	-2.616
				-2.106	-2.106	-2.616
Mg	4th	4.755	+1.71	0.000	0.000	-4.755

Table S8: Distance from the Ln adatom, Bader charges and atomic coordinates for the atoms composing the first three coordination shells around the Ln, for a Dy adatom on the bridge adsorption site on MgO.

Atom	Shell	Distance (in Å)	Bader Charge (in e^-)	Cartesian Coordinates x (Å)	y (Å)	z (Å)
Dy	-	-	+0.24	0.000	0.000	0.000
O	1st	2.603	-1.72	-1.004	-1.004	-2.182
				1.004	1.004	-2.182
Mg	2nd	2.985	+1.66	-1.133	1.133	-2.518
				1.133	-1.133	-2.518
Mg	3rd	4.105	+1.70	-1.042	-3.159	-2.406
				-3.159	-1.042	-2.406
				3.159	1.042	-2.406
				1.042	3.159	-2.406

Table S9: Distance from the Ln adatom, Bader charges and atomic coordinates for the atoms composing the first four coordination shells around the Ln, for a Ho adatom on the top-O adsorption site on MgO.

Atom	Shell	Distance (in Å)	Bader Charge (in e^-)	Cartesian Coordinates x (Å)	y (Å)	z (Å)
Ho	-	-	+0.11	0.000	0.000	0.000
O	1st	2.258	-1.66	0.000	0.000	-2.258
Mg	2nd	3.380	1.68	0.000	2.174	-2.588
				2.174	0.000	-2.588
				0.000	-2.174	-2.588
				-2.174	0.000	-2.588
O	3rd	3.931	-1.71	2.105	2.105	-2.568
				2.105	-2.105	-2.568
				-2.105	2.105	-2.568
				-2.105	-2.105	-2.568
Mg	4th	4.707	+1.71	0.000	0.000	-4.707

Table S10: Distance from the Ln adatom, Bader charges and atomic coordinates for the atoms composing the first four coordination shells around the Ln, for a Ho adatom on the bridge adsorption site on MgO.

Atom	Shell	Distance (in Å)	Bader Charge (in e^-)	Cartesian Coordinates x (Å)	y (Å)	z (Å)
Ho	-	-	+0.15	0.000	0.000	0.000
O	1st	2.666	-1.71	-1.012	-1.012	-2.249
				1.012	1.012	-2.249
Mg	2nd	3.006	1.67	-1.122	1.122	-2.553
				1.122	-1.122	-2.553
Mg	3rd	4.138	1.70	-1.048	-3.164	-2.453
				-3.164	-1.048	-2.453
				3.164	1.048	-2.453
				1.048	3.164	-2.453

Crystal field point charges for multiplet calculations

Table S11: Point charges used to simulate the CF for Dy and Ho adatoms at different adsorption sites on BaO (top-O, bridge-x and bridge-y) in multiplet simulations.

Dy^{top}

x, Å	y, Å	z, Å	q, e^-
0.000	0.000	−1.540	−0.360
1.270	1.270	−1.600	1.360
1.270	−1.270	−1.600	1.360
−1.270	1.270	−1.600	1.360
−1.270	−1.270	−1.600	1.360
0.000	0.000	−3.770	1.387

Ho^{top}

x, Å	y, Å	z, Å	q, e^-
0.000	0.000	−1.540	−0.2835
1.270	1.270	−1.600	1.360
1.270	−1.270	−1.600	1.360
−1.270	1.270	−1.600	1.360
−1.270	−1.270	−1.600	1.360
0.000	0.000	−3.770	1.387

$Dy^{br\text{-}x}$

x, Å	y, Å	z, Å	q, e^-
1.150	0.000	−1.090	−0.520
−1.150	0.000	−1.090	−0.520
0.000	1.260	−1.150	1.300
0.000	−1.260	−1.150	1.300

$Ho^{br\text{-}x}$

x, Å	y, Å	z, Å	q, e^-
1.150	0.000	−1.090	−0.560
−1.150	0.000	−1.090	−0.560
0.000	1.260	−1.150	1.300
0.000	−1.260	−1.150	1.300

$Dy^{br\text{-}y}$

x, Å	y, Å	z, Å	q, e^-
0.000	1.150	−1.090	−0.520
0.000	−1.150	−1.090	−0.520
1.260	0.000	−1.150	1.300
−1.260	0.000	−1.150	1.300

$Ho^{br\text{-}y}$

x, Å	y, Å	z, Å	q, e^-
0.000	1.150	−1.090	−0.560
0.000	−1.150	−1.090	−0.560
1.260	0.000	−1.150	1.300
−1.260	0.000	−1.150	1.300

References

[1] Heilmann, P.; Heinz, K.; Müller, K. The Superstructures of the Clean Pt(100) and Ir(100) Surfaces. *Surf. Sci.* **1979**, *83*, 487–497.

[2] Abernathy, D. L.; Mochrie, S. G. J.; Zehner, D. M.; Grübel, G.; Gibbs, D. Orientational epitaxy and lateral structure of the hexagonally reconstructed Pt(001) and Au(001) surfaces. *Phys. Rev. B* **1992**, *45*, 9272–9291.

[3] Mortensen, J. J.; Linderoth, T. R.; Jacobsen, K. W.; Lægsgaard, E.; Stensgaard, I.; Besenbacher, F. Effects of anisotropic diffusion and finite island sizes in homoepitaxial growth: Pt on Pt(100)-hex. *Surf. Sci.* **1998**, *400*, 290–313.